JOURNAL OF GEOPHYSICAL RESEARCH, VOL. 114, C00B12, doi:10.1029/2008JC005036, 2009

Structure and composition of a strongly stratified, tidally pulsed river plume

Jonathan D. Nash,[1] Levi F. Kilcher,[1] and James N. Moum[1]

Received 21 July 2008; revised 20 January 2009; accepted 10 April 2009; published 14 August 2009.

[1] The initial composition of a river plume depends on the cumulative turbulent entrainment within the estuary and how this dilutes the supplied freshwater. Here we examine the relative roles of turbulence and freshwater input using observations from the Columbia River estuary and plume during two periods with contrasting river flow. Within the estuary, intense turbulence observed on flood and ebb stages is controlled by the bottom stress and scales with tidally dominated near-bottom velocity as u_{tidal}^3. Shear associated with the estuarine circulation is found to have a much weaker influence on turbulence dissipation rates. On the basis of these observations, we suggest that properties of the Columbia River tidal plume should be controlled by the ratio of horizontal advection to turbulent mixing within the estuary. This ratio depends on the magnitude of freshwater river input (characterized by its volumetric flow rate Q_f) as compared to turbulent fluxes due to tidal mixing. This is summarized in terms of the estuary Richardson number Ri_E, a nondimensional ratio between Q_f and u_{tidal}^3. From 17 tidally resolving offshore surveys during spring/neap tides and low/high river flows, we find that the plume's median salinity, thickness, and turbulent mixing are each predicted through Ri_E. It is hoped that these simple formulations will provide guidance in assessing critical properties of river plumes and their influence on coastal circulation.

Citation: Nash, J. D., L. F. Kilcher, and J. N. Moum (2009), Structure and composition of a strongly stratified, tidally pulsed river plume, *J. Geophys. Res.*, *114*, C00B12, doi:10.1029/2008JC005036.

1. Introduction

[2] The Columbia River represents three quarters of the freshwater input to the Pacific Ocean from the United States West Coast. It issues as strongly stratified tidal pulses which are initially connected to the bottom, but ultimately detach and spread as highly sheared buoyant gravity currents. The location of the transition region (or lift-off point) depends on the tidal stage, moving progressively seaward as ebb flow strengthens, and back into the river mouth after tidal reversal [*Jay and Smith*, 1990a]. The structure and timing of the gravity current are highly variable and depend on a combination of the strength of the tidal discharge, the diurnal inequality, and how the gravity current interacts with plume remnants from previous tidal cycles (L. Kilcher and J. D. Nash, Evolution of the Columbia River tidal plume front, manuscript in preparation, 2009). On longer time scales, the gravity current relaxes and may radiate nonlinear internal waves [*Nash and Moum*, 2005]; it becomes influenced by the Earth's rotation, and its fate is dictated largely through interaction with preexisting coastal currents and the wind [*Lentz*, 2004; *Fong and Geyer*, 2001]. During the appropriate conditions, this offshore plume may form a slowly rotating bulge [*Horner-Devine*, 2009] that is semistationary (i.e., weakly influenced by the tides) and recirculates its fluid.

[3] Upstream of the lift-off point, the plume/river system is strongly constrained by the finite water depth, which effectively sets the depth-averaged velocity shear and drives the system to near-critical gradient Richardson number ($Ri = N^2/S^2 \approx 1/4$) [*Geyer and Smith*, 1987]. During ebb and flood, turbulence often spans the full water column and creates a partially mixed estuary which is strongly influenced by both tides and river inputs. Because of the strong tidal currents and intense shear, turbulent transports within the estuary are significantly higher than within the offshore plume, so a large fraction of the river's mixing occurs within the estuary. Hence, we hypothesize that turbulence dynamics in this region control the composition and structure of fluid leaving the estuary. Since most coastal numerical models do not explicitly resolve the estuary dynamics, quantifying the salinity, volume flow rate, and vertical structure of a river discharge near its mouth is important.

[4] Moreover, estuary-driven entrainment establishes the initial density and thickness of the near-field gravity current, which helps set the composition of the plume far field [*Horner-Devine et al.*, 2008]. This initial entrainment also provides a sufficient influx of nutrients and planktonic seed populations to allow for almost unrestricted initial growth in the rapidly evolving biological communities [*Kudela and Peterson*, 2009]. Many physical aspects of the far-field plume are also sensitive to the initial plume buoyancy g' and thickness h, such as its response to wind [i.e., *Lentz*,

[1]College of Oceanic and Atmospheric Sciences, Oregon State University, Corvallis, Oregon, USA.

0148-0227/09/2008JC005036$09.00

2004; *Fong and Geyer*, 2001] and its influence on biological productivity through the availability of light and nutrients [i.e., *Lohan and Bruland*, 2006].

[5] A number of recent studies have directly measured the structure of turbulence within estuaries. In the Hudson, direct observations [*Trowbridge et al.*, 1999; *Geyer et al.*, 2000; *Peters and Bokhorst*, 2000, 2001] and dye studies [*Chant et al.*, 2007] have documented the structure of stress and turbulence, leading to a better understanding of the circulation and salt budget there [*Lerczak et al.*, 2008]. *Stacey et al.* [1999] used an ADCP variance technique to describe the evolution of turbulence in the partially mixed San Francisco Bay. In these studies, mixing within the stratified interior was generally found to be linked to the tidally dominated bottom stress. However, strain-induced asymmetries were shown to strongly alter the partitioning of mixing between flood and ebb stages [*Stacey and Ralston*, 2005; *Li et al.*, 2008]. In the Columbia River, *Kay and Jay* [2003] made direct observations of dissipation rates and eddy fluxes during neap tides and found enhanced interior mixing at the top of the salt wedge during ebb. Control volume approaches [*MacDonald and Geyer*, 2004] have also been used to indirectly quantify turbulence in the Fraser River; *MacDonald and Horner-Devine* [2008] later combined these with Thorpe analyses to confirm the dominance of the vertical salt flux term in the salt budget.

[6] However, few studies have captured both turbulence within an estuary while also measuring the resultant fine-scale plume structure. Here it is our objective to assess how advection and mixing control the composition and structure of an offshore plume under a variety of river flows and tidal forcings. We combine 2 detailed estuary time series with 17 tidally resolving offshore surveys to show that the salinity in the near-field Columbia River plume is largely controlled by the estuary Richardson number (Ri_E) [*Fischer*, 1972], which we suggest describes the balance between horizontal advection and vertical mixing. Because Ri_E is based only on the river flow and tidal strength, this may be useful in predicting river plume composition on the basis of external parameters alone.

[7] Our paper is organized as follows. First we describe our instrumentation and methods (section 2). We then characterize the structure of mixing and mean flow for low– and high–river flow periods (section 3). These data are used to compute turbulent and advective freshwater fluxes in section 4. In section 5 we quantify the composition, structure and turbulence of the near-field plume, and examine its relationship to tidal strength and river flow. In section 6, we relate plume properties to Ri_E. Conclusions are presented in section 7.

2. Methods

[8] In the following we use shipboard observations from the R/V *Pt. Sur* to examine the structure of stratification, shear and turbulence within the Columbia River estuary and near-field plume during two time periods with dramatically different river discharges. During August 2005, weak river flows ($\sim$4000 m^3 s^{-1} at Beaver Dam) produced a thick and salty plume (20–25 practical salinity units (psu)). This contrasts the high flows (12,000 m^3 s^{-1}) during May 2006 which resulted in a thin and fresh plume (5–15 psu).

[9] The loosely tethered *Chameleon* microstructure profiler was used to obtain highly resolved profiles of temperature T, salinity s, density ρ, turbulent shear du'/dz, suspended sediment concentration (*SSC*) (determined from 880 nm optical backscatter as described by E. Spahn et al. (Particle resuspension in the Columbia River plume near-field, submitted to *Journal of Geophysical Research*, 2008)), and chlorophyll fluorescence *FLR*. To avoid contamination from the ship's wake, the profiler was tethered from the end of the ship's crane, about 5 m outboard and fore of the ship's starboard stern quarter. Vertical profiles were obtained from surface to within 10 cm of the bottom every 2 min, with the profiler nominally free-falling at 1 m s^{-1}. The turbulent kinetic energy dissipation rate ϵ was computed from two orthogonally mounted shear probes as described by *Moum et al.* [1995]. Useful dissipation measurements were not obtained within the upper 3 m, where the profiler was rapidly accelerating and changing orientation. In addition, contaminated ϵ data were identified during periods when the ship orientation, drift, and water column shear combined to place the profiler in the ship's wake; for short periods, this affected data down to 8-m depths. Vibrationally contaminated ϵ data were also identified using onboard accelerometers.

[10] To capture as much of the near-surface plume as possible, shipboard acoustics were deployed at 1.3-m water depth on over-the-side pole mounts. Water column velocities in the upper 25 m were obtained using a bottom-tracked 1200 kHz RD Instruments ADCP (starboard mount, 0.5-m bins, 10 pings s^{-1}). This was supplemented with a hull-mounted 300 kHz RDI unit (1-m bins, bottom tracked) to provide velocities down to O(100 m). In the following we compute the total shear-squared ($S^2 = (du/dz)^2 + (dv/dz)^2$) from 60-s averaged 1200 kHz data, and has approximately 1-m vertical resolution. To compute horizontal advection (section 4), ADCP velocities are extrapolated to the surface using a linear fit over 2.5 m $< z <$ 4.5 m, where z represents distance from the surface. A 120 kHz Biosonics echosounder (port mount) was used to image acoustic backscatter layers from both turbulence and biology.

[11] Time series within the estuary were nominally acquired at 46°15.3′N, 124°1.0′W, about 1 km north of the main shipping channel (station E) (Figure 1). However, maintaining a fixed station in six knot currents is challenging (especially without a bow thruster), so these data are spatially aliased to some unknown extent. Regardless, 90% of the estuary data were acquired within 300 m (E-W) and 160 m (N-S) of the desired location. 30-h time series were acquired during both 17–18 August 2005 and 23–24 May 2006, providing 2300 vertical profiles of turbulence used in the following analysis. While nearly continuous time series were acquired during 2005, an instrument failure on 24 May 2006 interrupted data collection for several hours; data are supplemented with shipboard conductivity-temperature-depth profiles during that period.

[12] In addition to the estuary time series, more than 300 transects were obtained at O(1 h) intervals along our main N-S (line 1) and E-W (line 4) sampling lines in the plume near field. These lines capture the plume's cross- and along-axis structure. On the basis of the analysis of these, data obtained within 1 km of these lines' intersection (at 46°14.4′N, 124°9.0′W, hereafter referred to as station P) is

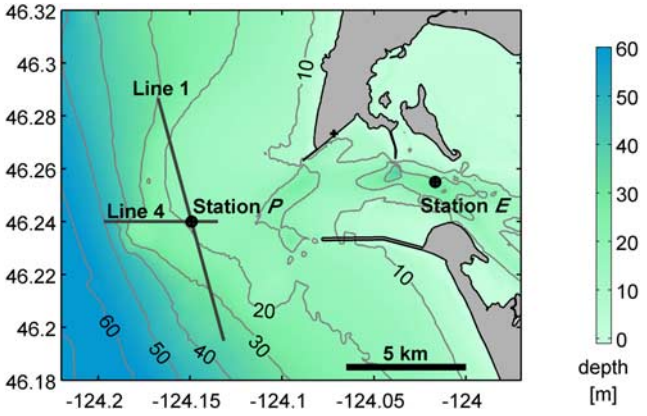

Figure 1. Bathymetry near the mouth of the Columbia River (10-m contour intervals). Locations of estuary and plume time series are indicated (dots), as are locations of repeated N-S and E-W transects from which the plume series were derived (straight gray lines). The North Jetty tide station is also indicated (cross).

considered representative of the near-field plume. Observations span 8–26 August 2005 and 22–31 May 2006, and include a range of upwelling, downwelling, high/low river flow, and phase within the spring/neap cycle (see B. Hickey et al. (River influences on shelf ecosystems: Introduction and synthesis, submitted to *Journal of Geophysical Research*, 2009) for more context).

[13] Throughout the paper, along-channel and along-axis directions are equivalent and defined as positive Eastward; all times are in UTC. Nominal tidal elevations η_o have been computed for the North Jetty (46°16.40′N, 124°4.30′W) using XTide harmonic predictions. Tidal cycle averages and temporal integrals are computed using trapezoidal integration of quasi-regularly spaced data.

3. Estuary Structure

3.1. Basic Flow Description

[14] A 24.8-h time series from 17 to 18 August 2005 (Figure 2) illustrates the typical flow evolution at the estuary station E during low river flow (4000 m^3 s^{-1}) and a moderate ebb tide with strong diurnal inequality (cycle includes a 1- and 3-m tidal drop at the North Jetty). Because the tidal excursion and the length of the salinity intrusion are both O(20 km) in the Columbia River estuary [*Jay and Smith*, 1990a], our time series samples a large fraction of the salt wedge as it advects past our station, particularly during the greater ebb/flood. During the lesser ebb and flood, low-s water never reaches the bottom, so only the seaward part of the salt wedge passes our site.

[15] At high water (1900 and 0630 UTC), the water column is mostly of oceanic salinity ($s \sim 33$ psu) and contains only thin (<5 m) remnants of sub-28 psu plume water that were pulled back into the estuary during flood. Shortly after high tide (2000 and 0730), the flow reverses in a barotropic sense; water column shear weakens considerably as does ϵ. During these periods, the entire water column is relatively quiescent.

[16] After the onset of ebb flow (2100 and 0900), the water column becomes progressively more stratified. A near-surface layer of fresh water emerges, producing high stratification that supports intense shear, complex fine structure, and strong turbulence. At this time, numerous fronts and wave-like features are evident throughout the water column. However, despite the emergence of high upper water column S^2, the strongest turbulence is driven by near-bottom processes, where the stratification is weaker. There, even modest S^2 can lead to highly unstable Ri. In contrast, upper column N^2 generally hovers near $S^2/4$, so that fluid there is only marginally unstable and turbulence limited by the stratification.

[17] We use a density criterion to define the thickness of the well-mixed bottom boundary layer, such that h_{bbl} represents the upper boundary of fluid within $\Delta\sigma = 0.05$ kg m^{-3} of the maximum density. While h_{bbl} is a measure of the near-bottom mixed layer based on an $N^2 \rightarrow 0$ or $Ri \ll 1/4$ criterion (Figure 2e), it rarely caps the region of high ϵ (Figure 2f) which penetrates well above h_{bbl} and into the increasingly stratified interior where $Ri \approx 1/4$ (e.g., 0300–0600 and 0900–1200). As a result, $\epsilon(z)$ exhibits no discontinuity at h_{bbl}, but instead decays into the interior approximately as z^{-1} (i.e., following law-of-the-wall scaling for an unstratified fluid; not shown here). Our definition of h_{bbl} thus reflects the state of the estuary circulation (i.e., thick bottom boundary layers (BBLs) coincide with intrusion of high-salinity ocean fluid), as opposed to representing the upper boundary of a turbulent layer.

[18] Unlike the almost quiescent slack tide following high water, the reversal from ebb to flood (0100 and 1600) is strongly stratified and remains considerably sheared, supporting increased ϵ within the water column (i.e., at 0000, 20 m above bottom (mab) and at 1630, 15 mab). However, this upper water column turbulence is weak compared to that generated simultaneously near the bottom. Again, this results because S^2 and N^2 generally covary in the stratified interior, and are maintained near $Ri \approx 1/4$. This results in weaker turbulence in the interior as compared to that in the well-mixed BBL which is directly forced by the bottom stress. As a result, depth-averaged dissipation rates are dominated by near-bottom turbulence which peaks twice per tidal cycle (on both ebb and flood). This is similar to that found by *Peters* [1997] and *Peters and Bokhorst* [2000] in the Hudson River estuary.

[19] The asymmetry in the cycle of u and s at station E exhibits characteristics associated with tidal straining and internal tidal asymmetry [*Simpson et al.*, 1990; *Jay*, 1991], whereby shear associated with the tidal flow acts on horizontal density gradients to increase stratification during ebb and destroy it during flood. *Simpson et al.* [1990] used tidal straining to explain the internal structure in Liverpool Bay, and *Jay and Musiak* [1996] used internal asymmetry to explain the strong observed mean flow and internal overtides in the Columbia, using data collected 10 km landward of the present site. The same concept has also been applied to the Hudson [i.e., *Geyer et al.*, 2000] and numerous other estuaries. The time series at station E (Figure 2) also exhibits strain-induced asymmetries, as S^2 and N^2 increase during ebb and produce a highly sheared transition to flood. During flood, S^2 and N^2 decrease, so that the reversal to ebb is barotropic, devoid of shear.

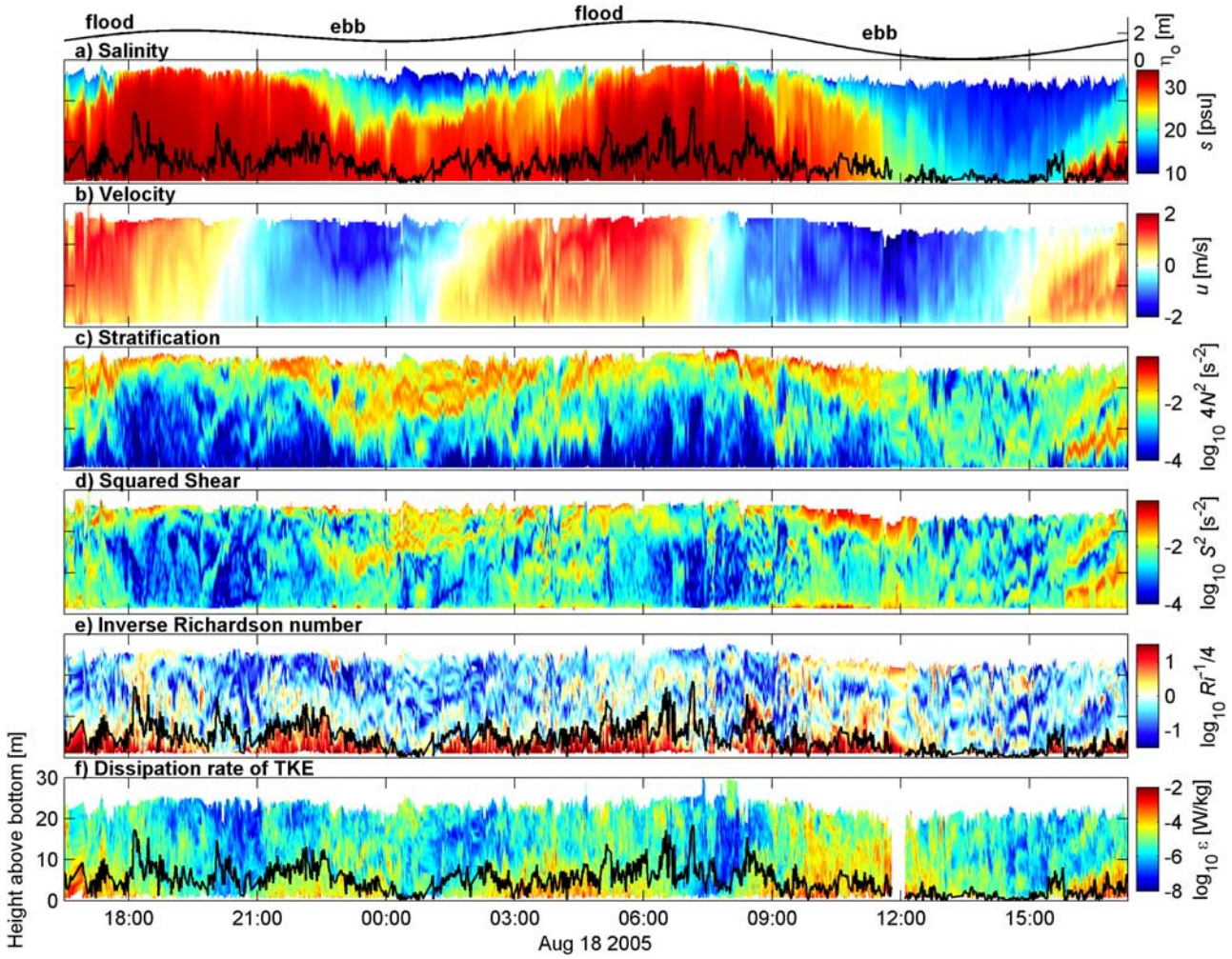

Figure 2. (a) Salinity, (b) along-channel velocity, (c) 4 times stratification, (d) squared shear, (e) inverse *Ri*, and (f) turbulence dissipation rate at station E during 17–18 August 2005. Data are plotted with respect to height above bottom, and profile to profile changes in the vertical extent of data thus reflect changes in the bottom depth (due to ship location). The trend represents the 3-m surface tide (η_o) (shown above Figure 2a). The bottom boundary layer height h_{bbl} is shown in Figures 2a, 2e, and 2f (black line). Times are in UTC.

[20] While our estuary observations are too short to quantify tidal asymmetries in mixing, we note here that dissipation rates at station E appear to be stronger during ebbs than floods, presumably a result of increased S^2 associated with the river flow, similar to that in the Fraser River [*Geyer and Smith*, 1987]. While somewhat anecdotal, it contrasts some previous studies [i.e., *Peters and Bokhorst*, 2001; *Stacey and Ralston*, 2005; *Li et al.*, 2008] that have generally linked increased turbulence with weak or unstable stratification during flood and suppressed turbulence with the more stable ebbs. However, other factors in addition to tidal asymmetry also affect flow structure, specifically the O(20 km) tidal excursion combined with our station's 5-km proximity to the river mouth. Because of the sharp horizontal gradients near the river mouth, tidal advection transports the salt wedge seaward during ebb, while it may bring ocean water of completely different origin into the estuary during flood.

3.2. Comparison Between Low– and High–River Flow Periods

[21] We contrast the time evolution of along-channel velocity, shear, and turbulence for low- and high-flow periods (August 2005 versus May 2006) in Figure 3. While the surface tides (Figures 3i and 3j) exhibited a stronger diurnal inequality on 18 August 2005 as compared to 24 May 2006, the power associated with the barotropic tide, as approximated by a 24.8-h average of $(d\eta_o/dt)^2$, differs by less than 3% between these two occupations. Thus although the estuarine structure of density and turbulence can be altered from subtle changes in diurnal inequality, we suggest the differences in tidal forcing are small compared to the changes in Q_f. We hence attribute differences in estuary structure between field seasons to be mostly a consequence of the threefold increase in river input during 2006, with changes in tidal forcing having secondary importance.

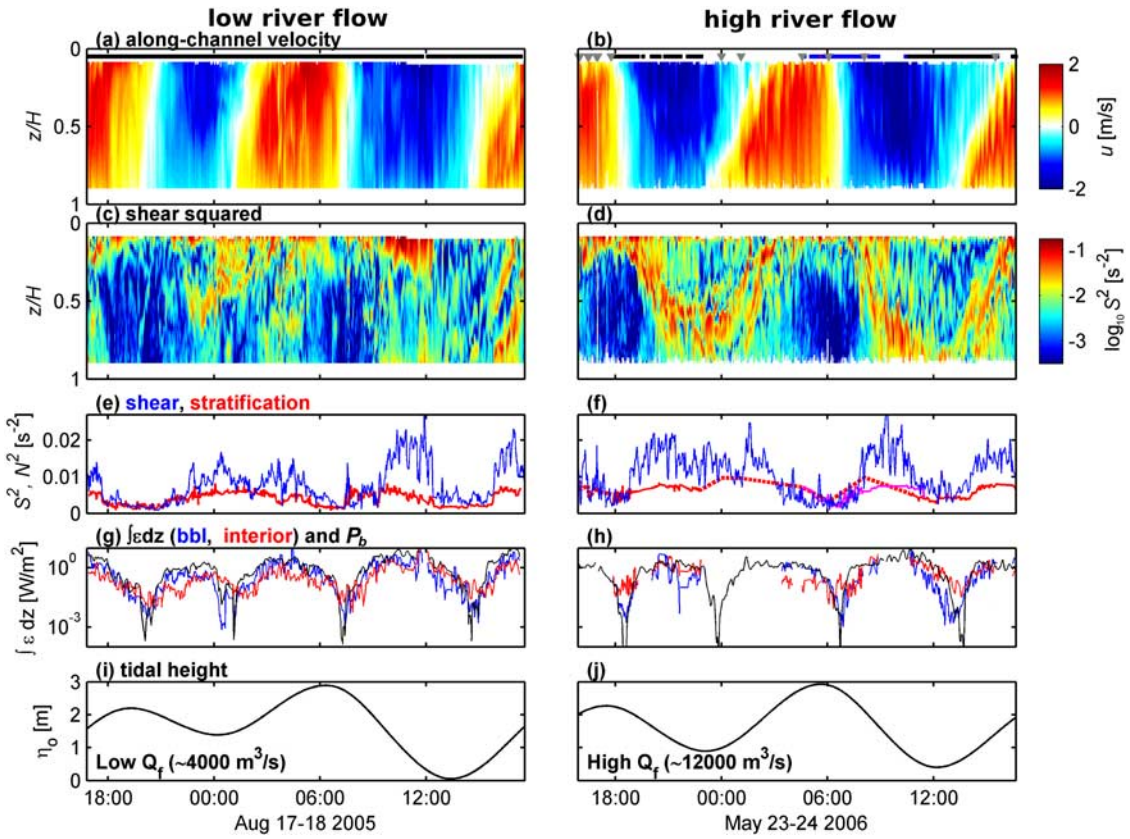

Figure 3. Two 24.8-h time series of (a, b) along-channel velocity and (c, d) squared shear during 17–18 August 2005 ((left) low river discharge) and 2006 ((right) high river discharge) at station E. (e, f) Depth averages of S^2 (blue, from 2.35 m below surface to 3 m above the bottom) and N^2 (red, full depth) are also presented. (g, h) TKE dissipation rates are shown for vertical integrals over the unstratified BBL (blue) and the stratified interior (red), defined as the remainder of the water column. For reference, the rate of work done by the bottom stress assuming a quadratic drag law ($P_b = \rho C_D u_5^3$) is shown in black. (i, j) The nominal surface tide at the North Jetty is shown for reference. Black horizontal bars in Figures 3a and 3b indicate periods of turbulence profiling. Shipboard conductivity-temperature-depth profiles (gray triangles in Figure 3b and red dashes in Figure 3f) are used to better define N^2 during 2006. In addition, N^2 computed from turbulence profiler data from the previous tidal cycle is shown in magenta in Figure 3f; these data are shifted in time by 24.8 h and also represented as a blue bar in Figure 3b. Dissipation data from the previous tidal cycle have also been added in Figure 3h for this time period (0300–0800).

[22] The velocity structure during 2006 is qualitatively similar to 2005 (as described above). Despite the slightly reduced tidal drop of the greater ebb in 2006, the maximum velocities during ebb flow are stronger, presumably owing to the increased river input. The asymmetry between slack tides at high and low water occurs in both years, with the transition from flood to ebb being almost completely barotropic and devoid of lower column S^2. This differs from the transition from ebb to flood, which is more intensely sheared, especially under high–river flow conditions (compare Figures 3a and 3b at 0000–0300), which produced extended periods (up to 4 h) where surface and bottom waters flowed in opposite directions. Under low–river flow conditions, reversed currents last only ~2 h.

[23] The most obvious consequence of high freshwater input is the localization and clear vertical migration of S^2 in 2006 that is not evident in 2005. The strongest shear is trapped to regions of high stratification, and moves vertically through the water column as the salt wedge is advected past our fixed station. This is particularly evident beneath the freshwater outflow during both ebb and the transition from ebb to flood (i.e., 2000, 23 May to 0300, 24 May 2006). In contrast, during 2005 regions of intense upper column shear are much more sporadic because of the much-reduced stratification; examples include high-S^2 patches near 0000 and 1100, 18 August 2005. We note that some of the year-to-year differences may be associated with a shift in the mean location of the salt wedge, which moves seaward during high river flows, and inland during weak Q_f. Thus, our time series station effectively samples a different part of the estuary circulation during each field season.

[24] The influence of river flow on the turbulence structure is quantified using time series (Figures 3e–3h) and time averages (Table 1) of depth-averaged S^2, depth-averaged N^2 and depth-integrated dissipation. During high Q_f (Figure 3f), the 24.8-h mean $\overline{S^2}$ is 40% higher than that during low Q_f (Figure 3e). However, this is offset by $\overline{N^2}$, which increases by more than 70% during high Q_f. As a result, the mean $\overline{S^2}/\overline{N^2}$ is 20% lower during the period of high river flow (Table 1).

Table 1. Cycle-Averaged Properties at Station E[a]

	17–18 Aug 2005	23–24 May 2006
$\overline{Q_f}$ ($m^3\ s^{-1}$)	4,000	12,000
$\overline{N^2}$ (s^{-2})	3.9×10^{-3}	6.7×10^{-3}
$\overline{S^2}$ (s^{-2})	7.6×10^{-3}	10.7×10^{-3}
$\overline{S^2}/\overline{N^2}$	2.0	1.6
BBL $\int_0^{h_{bbl}} \epsilon dz$ ($W\ m^{-2}$)	0.97	0.52
Interior $\int_{h_{bbl}}^{H+\eta_o} \epsilon dz$ ($W\ m^{-2}$)	0.53	0.72
Total $\int_0^{H+\eta_o} \epsilon dz$ ($W\ m^{-2}$)	1.50	1.24
Drag law $P_b = \rho C_D u_5^3$ ($W\ m^{-2}$)	1.56	1.26
Interior Ozmidov $\langle \ell_o \rangle$ (m)	0.25	0.18
h_{bbl} (m)	4.8	4.4
$\overline{uF}$ ($m\ s^{-1}$)	−1.83	−7.46
$\overline{K_\rho dF/dz}$ ($m\ s^{-1}$)	-6.9×10^{-4}	-9.3×10^{-4}

[a]Properties correspond to the data and time periods shown in Figures 3e–3h. All quantities represent 24.8-h time averages; overbars denote depth averages.

3.3. Energy Dissipation

[25] On the basis of the interannual differences in S^2 and N^2 associated with the threefold increase in Q_f (Figure 3), one might expect significant changes in ϵ. However, tidal forcing clearly dominates the cycle of turbulence (Figures 3g and 3h). As in the Hudson [*Peters and Bokhorst*, 2001], turbulent kinetic energy (TKE) dissipation rates, integrated over either the BBL ($\int_0^{h_{bbl}} \epsilon dz$; blue) or stratified interior ($\int_{h_{bbl}}^{H+\eta_o} \epsilon dz$; red) exhibit maxima during ebb and flood. Dissipation rates also vary in accord with a one-dimensional, steady state energy balance, in which vertically integrated turbulence dissipation is balanced by the rate of work done by the bottom stress, $\mathbf{u} \cdot \boldsymbol{\tau}_\mathbf{b}$. If a quadratic drag law is assumed for τ_b, this yields a convenient result that the rate of work by the bottom is simply

$$P_b = \rho C_D u_5^3, \tag{1}$$

where u_5 is the velocity 5 m above the bottom. While this formulation neglects the work done by internal pressure gradients, it provides a useful scaling for bulk dissipation rates driven by barotropic processes. A value of $C_D = 1.8 \times 10^{-3}$ was used in this analysis.

[26] In the following, we consider the structure and partitioning between stratified and boundary turbulence during these two periods, with an aim at quantifying these in terms of a mean flow derived metric (i.e., P_b). This follows the approach taken by *Peters and Bokhorst* [2000, 2001], who found a general correspondence in the Hudson River estuary between turbulence within the stratified interior and the rate of working by the bottom stress. While they concluded that stratified shear instability was the likely mechanism of turbulence generation [i.e., *Geyer and Smith*, 1987], they suggested it to be forced indirectly by the bottom boundary layer, whereby instabilities extend into the stratified interior as a result of stress transmitted through the well-mixed region [*Trowbridge*, 1992]. *Stacey et al.* [1999] also attributed interior mixing in San Francisco Bay to a similar mechanism. On the other hand, *Kay and Jay* [2003] found substantial internal mixing to occur during periods of weak near-bed shear, suggesting the importance of stresses associated with internal processes. We find similar evidence of mixing associated with enhanced internal shear (i.e., within the low *Ri* near-surface waters during 0900–1200, 18 August (Figure 2)), but will show that depth averages of ϵ still scale with P_b.

[27] We first compute integrated turbulence dissipation rates both within and above the well-mixed bottom boundary layer, defined using h_{bbl}. The time series of h_{bbl} for 2005 is shown in Figure 2, and integrated dissipation rates in Figures 3g and 3h. Tidal cycle averages of these and P_b are summarized in Table 1. Under low Q_f, BBL dissipation is dominant, representing two thirds of the water column integrated ϵ in August 2005. Under high Q_f, dissipation in the stratified interior exceeds that in the BBL, likely because of increased $\overline{S^2}$. However, full depth-integrated dissipation rates are similar in both years because N^2 increases more than $\overline{S^2}$ under high Q_f, leading to an overall reduction in $\overline{S^2}/\overline{N^2}$ during 2006. Total integrated dissipation rates and the mean $\overline{S^2}/\overline{N^2}$ were both 20% lower during the high Q_f sampling in 2006.

[28] A significant fraction of the stratified interior tends to be marginally unstable, with typical $Ri \approx 1/4$. Hence the (S^2, N^2) parameter space in the estuary contrasts typical coastal environments, which tend toward stable *Ri*, except for regions of actively breaking large-scale waves [*MacKinnon and Gregg*, 2003; *Moum et al.*, 2003]. At station E, 30% of the data are associated with $Ri < 1/4$ during 2005, and these data account for 63% of the depth-integrated dissipation rate in the interior (i.e., corresponding to $\int_{h_{bbl}}^{H+\eta_o} \epsilon dz$ in Table 1). During 2006, 21% of the data have $Ri < 1/4$ and account for 46% of the integrated dissipation in the stratified interior. These percentages of $Ri < 1/4$ are very similar to the 22% $Ri < 1/4$ reported by *Geyer and Smith* [1987] within the pycnocline of the Fraser River estuary during ebb (note that Geyer and Smith's $\tilde{R}i$ based on the total shear is equivalent to our *Ri*). Hence, shear instability appears to be a dominant source of the turbulence within the interior.

[29] We further illustrate that the depth-integrated ϵ is dominated by bottom boundary processes as represented by a quadratic drag power loss P_b. Shown in the time domain in Figures 3g and 3h, we quantify this relationship following *Peters and Bokhorst* [2000] by comparing vertical integrals of ϵ to $P_b = \rho C_D u_5^3$ on a profile by profile basis in Figure 4. $\int \epsilon dz$ strongly covaries with P_b except at low u_5, corresponding to slack water. This mismatch may result from turbulence associated with mid–water column shear that exists despite $u_5 \sim 0$. Alternatively, boundary layer turbulence may persist through slack water because of large time scales for turbulence decay, which scales approximately with $1/N$.

[30] Given the marked year-to-year differences in S^2 and N^2 associated with changes in Q_f, the quantitative similarity in depth-integrated dissipation rate is striking, both between years (Figure 4) and between river systems (i.e., compare to Figure 8 of *Peters and Bokhorst* [2000] for the Hudson). This is somewhat surprising given the degree of upper water column stratification and relatively small Ozmidov scales (ℓ_o), which provides a measure of the scale of turbulent overturns [*Dillon*, 1982]. Median ℓ_o in the stratified interior is 0.18–0.25 m (Table 1), but has factor of 10 variability within the water column; ℓ_o is reduced in 2006 in accord with increased $\overline{N^2}$.

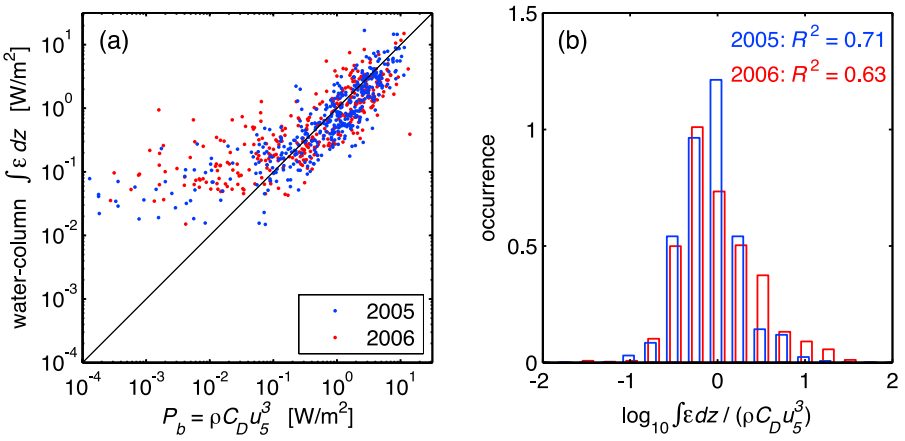

Figure 4. (a) Water column integrated dissipation versus the work done by bottom friction $P_b = \rho C_D u_5^3$ at station E. Each data point represents an average of three profiles (blue, August 2005; red, May 2006). (b) Histograms represent the log of the ratio of $\int \epsilon dz$ to P_b; periods of slack flow ($u_5 < 0.2$ m s^{-1}) have been omitted from the histograms and R^2.

[31] Increased stratification during 2006 clearly alters the partitioning of dissipation between BBL and stratified interior (Table 1), yet these differences are concealed by our presentation of full depth integrals in Figure 4. For example, integrated dissipation rates within the unstratified BBL are reduced by a factor of 2 during 2006, but this is compensated by a 35% increase in dissipation in the stratified interior. In both years, however, the cycle-averaged full water column $\int_0^{H+\eta_o} \epsilon dz$ is approximately equivalent to P_b (Table 1), despite the differences in partitioning.

[32] The relationship suggested by Figure 4 highlights the importance of tidal forcing in setting $\int_0^{H+\eta_o} \epsilon dz$, which scales with u_5^3 and thus P_b. As suggested by *Trowbridge* [1992], *Stacey et al.* [1999], *Peters and Bokhorst* [2000], and others, the bottom stress is a dominant control, even within the stratified interior. This occurs because stresses within the boundary layer are transmitted through the water column. Our results provide additional evidence for this, as we find that the interior dissipation may increase to compensate for decreased BBL dissipation during times of thin boundary layers; the stress is effectively acting on the stratified interior instead of within the mixed boundary layer. This contrasts other studies that find turbulence is suppressed by stratification; the difference is that the regions of high N^2 we observe are also associated with high S^2 that produces $Ri < 0.25$.

4. Freshwater Transports: Advective and Turbulent Fluxes

[33] The salinity of fluid exiting the river mouth is set by the cumulative effect of turbulent entrainment of salt water into a freshwater fluid parcel as it is advected from the river source. To quantify the effect of mixing, we define the freshwater fraction

$$F = (s_o - s)/s_o, \tag{2}$$

which represents the volume fraction of freshwater, which, when mixed with pure seawater of salinity $s_0 = 33$ psu, produces the observed salinity s. Hence, $F = 1$ represents pure river water and $F = 0$ represents pure seawater. We then define the horizontal advective flux of freshwater (i.e., freshwater advection) as $\mathcal{F}_{\text{adv}} = uF$ (units of m s^{-1}, representing m^3 of freshwater passing through a 1 m^2 area per second). The vertical turbulent freshwater flux is $\mathcal{F}_{\text{turb}} = K_\rho dF/dz$; note that $\mathcal{F}_{\text{turb}}$ is equivalent to $-1/s_o$ times the turbulent saltwater flux. The eddy diffusivity is computed from the TKE production-dissipation balance following *Osborn* [1980] as $K_\rho = \Gamma\epsilon/N^2$, where we assume $\Gamma = 0.2$ is the mixing efficiency; we set $K_\rho = 0$ in unstratified regions ($N^2 < 10^{-5}$ s^{-2}). $\mathcal{F}_{\text{turb}}$ was not estimated in the upper 3 m, where ϵ measurements were contaminated by ship wake.

[34] Vertical profiles of advective and turbulent fluxes of freshwater (time averaged over a 24.8-h period) are shown in Figure 5; depth integrals are summarized in Table 1. While freshwater is advected both seaward and landward during each tidal cycle; seaward fluxes during ebb dominated, leading to cycle-averaged seaward transports approximately proportional to the river flow Q_f (i.e., net transports in 2006 are approximately 4 times that in 2005.)

[35] In contrast to the strong year-to-year differences in freshwater advection, the year-to-year similarities in TKE dissipation rate are striking (i.e., Table 1 and Figure 4.) As a result, cycle-averaged values of $\mathcal{F}_{\text{turb}}$ at station E are similar in both years (Figure 5). The similarity in $\mathcal{F}_{\text{turb}}$ occurs because the turbulent buoyancy flux J_b scales with dissipation rate in the stratified part of the water column (i.e., $J_b \sim 0.2\epsilon$). In accord with slightly increased stratified dissipation ($\int_{h_{\text{bbl}}}^{H+\eta_o} \epsilon dz$) during 2006, $\int_0^{H+\eta_o} \mathcal{F}_{\text{turb}} dz$ also increased by approximately 35%; year-to-year differences were largely confined to the upper half of the water column.

[36] Because salinity within the estuary strongly depends on Q_f, both advective and turbulent fluxes within the estuary span different salinity classes during 2005 and 2006. These differences are quantified by computing water column integrals of $\mathcal{F}_{\text{adv}}$ and $\mathcal{F}_{\text{turb}}$, each binned with respect to salinity (Figure 6), i.e.,

$$\mathcal{F}_{\text{adv}}^{(s)}(s) = \frac{1}{\Delta s} \int_{z(s-\Delta S/2)}^{z(s+\Delta S/2)} \mathcal{F}_{\text{adv}} dz'. \tag{3}$$

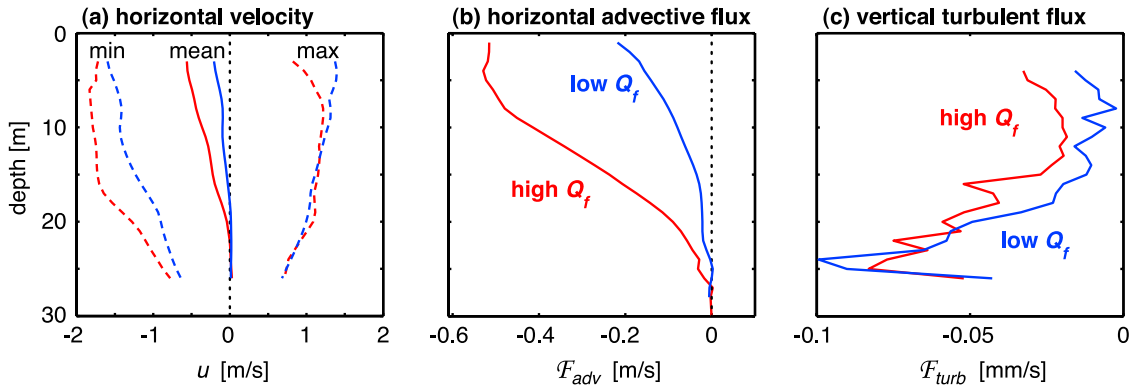

Figure 5. The 24.8-h cycle-averaged vertical profiles at station E of (a) horizontal velocity, (b) horizontal advective flux of freshwater $\mathcal{F}_{adv}$, and (c) vertical turbulent flux of freshwater $\mathcal{F}_{turb}$ for 2005 (blue) and 2006 (red).

$\mathcal{F}^{(s)}_{turb}$ is defined analogously. We compute $\mathcal{F}^{(s)}_{adv}$ and $\mathcal{F}^{(s)}_{turb}$ using Δs = 1 psu, producing 33 salinity classes. We then define $\bar{\bar{s}}$ as the salinity associated with the median of the cycle-averaged horizontal freshwater flux, $\langle \mathcal{F}^{(s)}_{adv} \rangle$; in other words, equal amounts of freshwater advection occurs above and below $\bar{\bar{s}}$. The median salinity $\bar{\bar{s}}$ is much lower during high Q_f, approximately $\bar{\bar{s}}$ = 4.9 psu during 2006 spring tides compared to $\bar{\bar{s}}$ = 16.4 psu during 2005 spring tides. In both years, most of the freshwater flux is carried by the freshest salinity classes.

[37] Diapycnal fluxes also shift to lower s in 2006 because (1) low-s water is in closer proximity to the bottom during high Q_f (where ϵ and $\mathcal{F}_{turb}$ are highest) and (2) upper water column $\mathcal{F}_{turb}$ is elevated during high Q_f. There is notable difference in distribution of the cycle-averaged $\langle \mathcal{F}^{(s)}_{turb} \rangle$ between 2005 and 2006. For low Q_f, most of the diapycnal flux occurs for s > 28 psu, fluid that is being transported up estuary on average, albeit weakly. In contrast, for high Q_f, $\langle \mathcal{F}^{(s)}_{turb} \rangle$ is distributed more broadly over all salinity classes, and almost all salinity classes have net offshore transports. These are due to the occurrence of high near-surface N^2 and S^2 during 2006, leading to increased upper column dissipation rates, and enhancing the turbulent buoyancy flux in the fresher water classes. Note, however, that in both years $\mathcal{F}_{turb}$ is not computed in the upper 3 m, so that diapycnal fluxes in the lowest salinity classes have been underestimated.

[38] We pause to caution drawing strong conclusions from small differences in $\mathcal{F}_{turb}$ and $\langle \mathcal{F}^{(s)}_{turb} \rangle$, which may not be significant given the uncertainties of our sampling. In particular, estimates are based on a single time series station within an estuary known to have strong lateral variability and along-estuary structure [*Jay and Smith*, 1990b]. Hence, in effect we are sampling different parts of the salt wedge in each year. Moreover, tidal averaging is inherently difficult in such settings. Finally, standard turbulence assumptions (i.e., isotropy, production-dissipation balance, constant mixing efficiency) preclude quantifying sub-50% absolute differences. We thus proceed using the above analysis for guidance but are cognizant of its limitations.

5. Consequences to the Near-Field Plume

[39] Our primary goal is to understand how the external forcing controls properties of the near-field tidal plume. In the following we describe the structure of freshwater transport and turbulence, using $\bar{\bar{s}}$ as a metric of its composition. We find that the tidal plume composition and structure vary systematically with Q_f and u^3_{tidal}.

5.1. Temporal Evolution of the Tidal Plume

[40] Turbulence profiler data collected in the near-field plume during August 2005 and May 2006 capture its time evolution and are used to assess the dependence of plume properties on river flow and tidal strength. Both along-plume (line 4) and cross-plume (line 1) transects (Figure 1) were obtained at hourly intervals for 17 12.4-h tidal cycles that span spring/neap tides, low/high Q_f, and upwelling/downwelling. A spatial analysis of the plume's structure

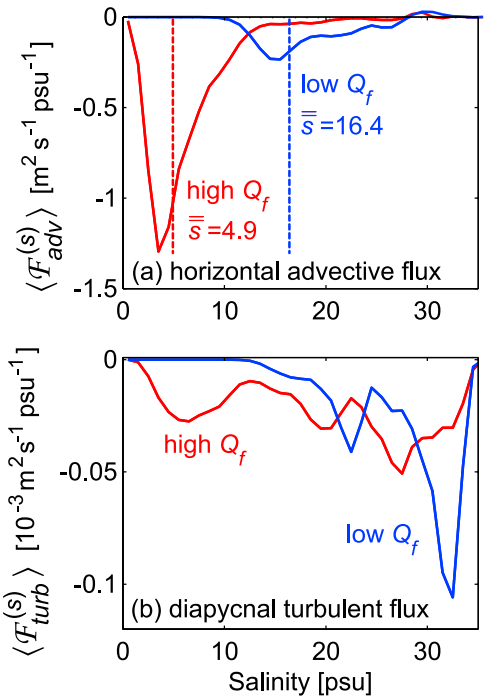

Figure 6. (a) Advective and (b) turbulent fluxes of freshwater during August 2005 (blue) and May 2006 (red) as a function of salinity class. Fluxes represent water column integrals at station E and have been time averaged.

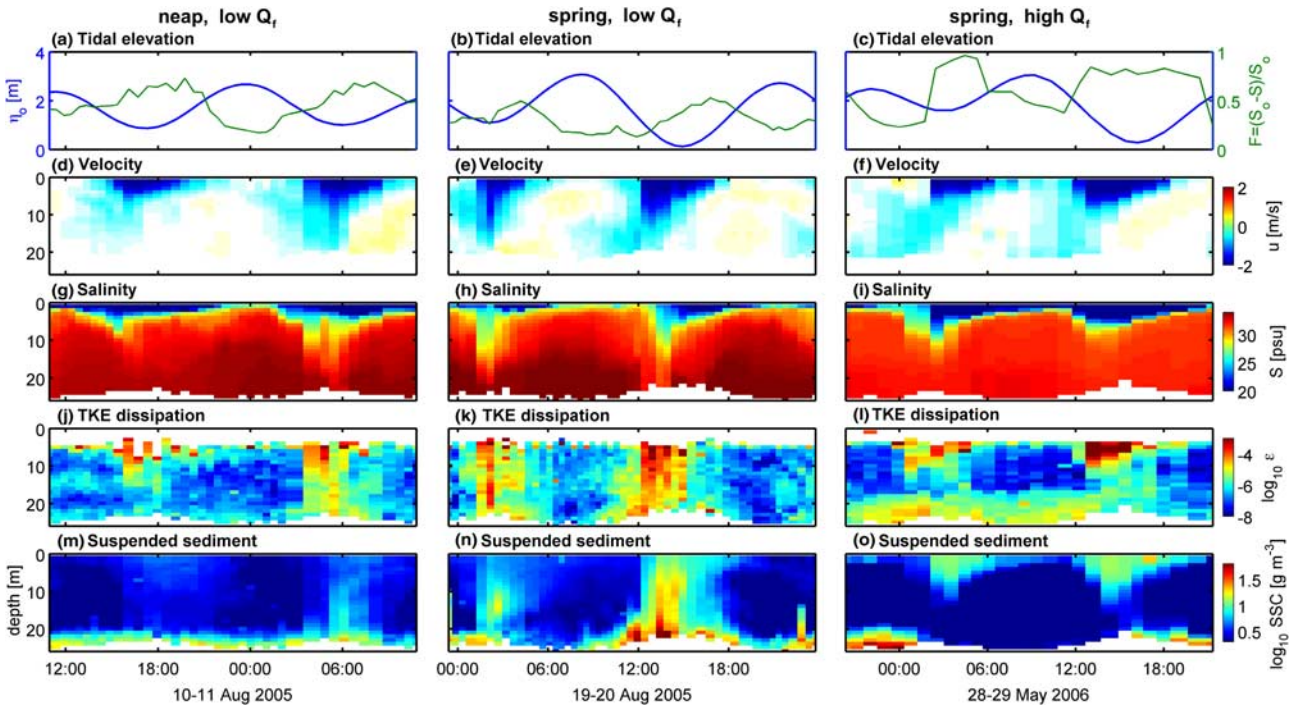

Figure 7. Virtual time series in the near field of the offshore plume for three different forcing states: (left) low Q_f, neap; (middle) low Q_f, spring; and (right) high Q_f, spring. Shown are (d–f) velocity, (g–i) salinity, (j–l) $\log_{10}\epsilon$, and (m–o) $\log_{10}SSC$ at station P. (a–c) Also shown are the time series of tidal elevation at the North Jetty (blue) and observed freshness in the upper 1 m (green).

derived from these transects (section 5.4) provides context and suggests that the lines' intersection (station P; 46°14.4′N, 124°9.0′W) is representative of the near-field plume. We begin by generating a virtual time series by combining profiler data obtained within 1 km of station P from each of >300 transects; typically 5–20 profiles were averaged at each time step.

[41] The temporal evolution at station P is shown in Figure 7 for three different forcings: low Q_f, neap; low Q_f, spring; high Q_f, spring. In each case, ebb currents arrive abruptly (Figures 7d–7f), emerging at station P slightly before low tide. The initial offshore pulse of fluid tends to be saltier than that which arrives later (green lines in Figures 7a–7c), producing weaker initial stratification than that later in the cycle. This allows initial ebb currents to penetrate deeper into the water column than those which follow. Peak velocities and dissipation rates depend on the amplitude of the surface tidal drop $\Delta\eta_o$, so are strongly influenced by the diurnal inequality.

[42] Despite these similarities in the time evolution, the plume's vertical structure varies considerably with both Q_f and tidal strength. During neap tides and low Q_f (Figure 7 (left)), the plume emerges thin and relatively fresh; contact with the bottom is weak, as indicated by ϵ and *SSC*. During spring tides and low Q_f (Figure 7 (middle)), the plume emerges much saltier because of the increased estuary mixing. It is less stratified and thicker, so that turbulence during both lesser and greater ebbs connects with the bottom and enables sediment resuspension (Spahn et al., submitted manuscript, 2008). During high Q_f and spring tides (Figure 7 (right)), the plume emerges fresh and thin. Plume turbulence is mostly confined within the upper 10 m and is intense. This time period also represents a case of downwelling, so ocean salinities are reduced because they represent a remnant mixture of ocean and plume water that is being downwelled and advected toward the river mouth. Because of weak stratification at depth, thick bottom boundary layers form which appear mostly disconnected from the tidal plume.

5.2. Freshwater Transport Within the Plume

[43] The time evolution of $\mathcal{F}_{\text{adv}}$ and $\mathcal{F}^{(s)}_{\text{adv}}$ for the greater ebb during spring tides and low Q_f (20 August 2005) is shown in Figure 8. This example represents the evolution of freshwater flux in both physical space and salinity space typical of a tidal pulse in the plume near field. The initial freshwater flux (1200–1300, 20 August) is carried by highly saline fluid (i.e., $s \approx 30$ psu) distributed throughout much of the water column. As the ebb strengthens, the peak $\mathcal{F}^{(s)}_{\text{adv}}$ shifts toward progressively fresher waters, with the majority of the flux at any given time being carried by the freshest salinity classes closest to the ocean surface. Peak freshwater transports occur near low water (1500, 20 August).

[44] As in the estuary, we quantify plume composition through $\bar{\bar{s}}$, the salinity associated with the median cycle-averaged freshwater flux. The distribution of $\langle\mathcal{F}^{(s)}_{\text{adv}}\rangle$ for the three cases shown in Figure 7 is shown in Figure 9. These show a shift toward fresher waters and a broadening of the distribution of $\langle\mathcal{F}^{(s)}_{\text{adv}}\rangle$ during periods of either high Q_f or weak tides, so that $\bar{\bar{s}}$ = 12.6 psu during 2006 spring tides compared to $\bar{\bar{s}}$ = 24.6 psu during 2005 spring tides. Such shifts in $\bar{\bar{s}}$ are at least intuitively consistent with the expected consequences of estuary turbulence as presented in

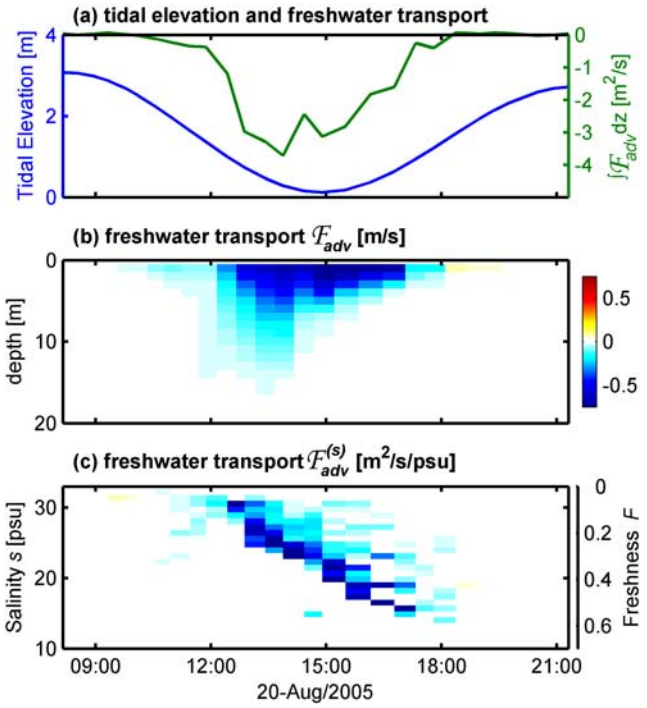

Figure 8. Temporal evolution of the distribution of freshwater flux in (b) physical space and (c) salinity space at station P during the 20 August 2005 greater ebb. (a) The tidal elevation (blue) and the vertically integrated freshwater flux $\int \mathcal{F}_{\mathrm{adv}} dvdz$ (green), which is also equivalent to $\int \mathcal{F}^{(s)}_{\mathrm{adv}} ds$.

section 3, resulting in increased freshness associated with either increased Q_f and/or decreased tidal mixing.

5.3. Vertical Structure of the Near-Field Plume

[45] We consider the three time periods shown in Figures 7 and 9 as representative examples of the different forcings: neap/low Q_f, spring/low Q_f and spring/high Q_f. During each of these periods, the vertical structure at station P is examined in terms of tidal cycle averages of $\mathcal{F}_{\mathrm{adv}}$, S^2, $4N^2$, ϵ and K_ρ (Figure 10).

[46] As also shown in Figures 7 and 9, spring tides and low Q_f produce a plume which is both thicker and saltier, so has weaker stratification and may be influenced by the bottom. This contrasts periods of neap tides or high Q_f, which result in strong near-surface N^2 and weak near-bottom turbulence (compare Figures 10d–10f to Figures 10a–10c and to Figures 10g–10i).

[47] As a metric of the near-field plume thickness, we compute the depth above which 80% or 95% of the freshwater flux $\langle \mathcal{F}_{\mathrm{adv}} \rangle$ is carried in a time-averaged sense, as indicated in Figures 10a, 10d, and 10g as h_{80} and h_{95}. As expected, during periods of neap tides or high Q_f, estuary dilution is weak and the near-field plume is fresh and thin ($h_{95} \approx 6$ m) (Figures 10a and 10g). In contrast, during spring tides and low Q_f, estuary dilution is strong and the plume emerges relatively salty and thick ($h_{95} \approx 11$ m) (Figure 10d).

[48] Turbulence dissipation rates ϵ were computed as averages over the period of ebb flow, defined as the duration over which the depth-integrated freshwater transport $\int \mathcal{F}_{\mathrm{adv}}\, dz$ exceeds 20% of its peak value (see Figure 8a). $\langle \epsilon \rangle$ is strongly surface intensified, being at least 2 orders of magnitude larger within the highly sheared, low-salinity plume waters than within the fluid beneath it. In general, the highest dissipation rates are associated with regions that are unstable in a mean sense (i.e., $\langle S^2 \rangle > \langle 4N^2 \rangle$) (Figures 10b, 10e, and 10h). In addition, during periods of high near-surface stratification (Figures 10b and 10h), the tidal plume has weaker vertical penetration, leading to near-bottom $\langle \epsilon \rangle \sim 10^{-6}$ W kg^{-1}, about a factor of 10 smaller than during periods of weak stratification, where near-bottom $\langle \epsilon \rangle > 10^{-5}$ W kg^{-1} (Figure 10f).

[49] Eddy diffusivities were computed from average vertical profiles of $\epsilon(z)$ and $N^2(z)$ at each station P occupation time step (i.e., 5–20 profiles within a 10–30 min interval were combined to form each $\epsilon(z)$) as $K_\rho(z) = 0.2\epsilon(z)/N^2(z)$. These were then averaged over the period of ebb flow to compute $\langle K_\rho \rangle$. As with $\langle \epsilon \rangle$, diffusivities are a factor of 10 higher during the period of spring tides and low Q_f, when the near-field plume penetrated through most of the water column. However, since ϵ tends to covary with N^2, stratification dependencies are somewhat removed by computing K_ρ. For example, the profiles of $\langle K_\rho \rangle$ are more similar in Figures 10c and 10i than their corresponding profiles of $\langle \epsilon \rangle$.

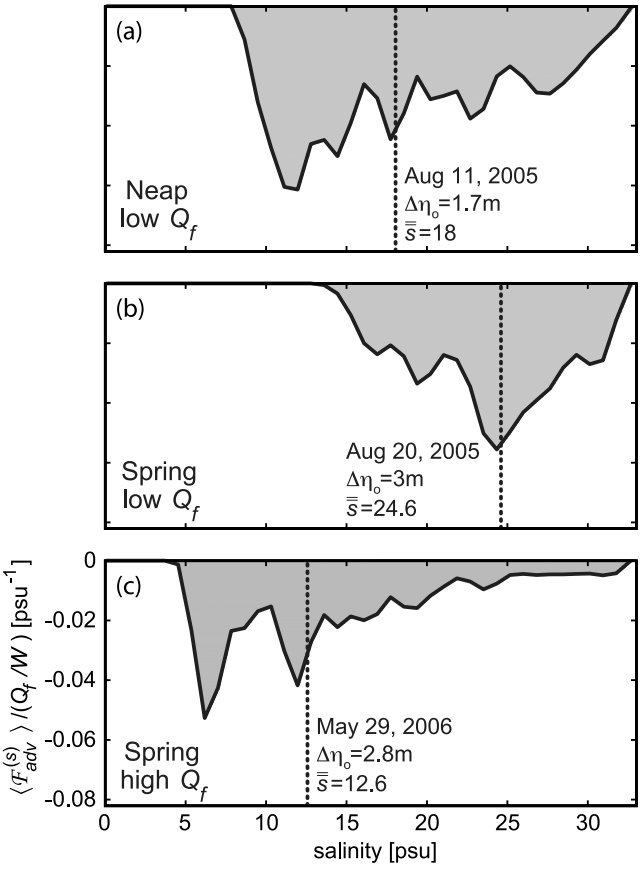

Figure 9. Cycle-averaged freshwater flux $\langle \mathcal{F}^{(s)}_{\mathrm{adv}} \rangle$ and the associated median salinity $\bar{\bar{s}}$ for the three periods shown in Figure 7. $\langle \mathcal{F}^{(s)}_{\mathrm{adv}} \rangle$ has been normalized by Q_f/W so that the area under each curve is approximately equal. The corresponding tidal drops are indicated as $\Delta\eta_o$.

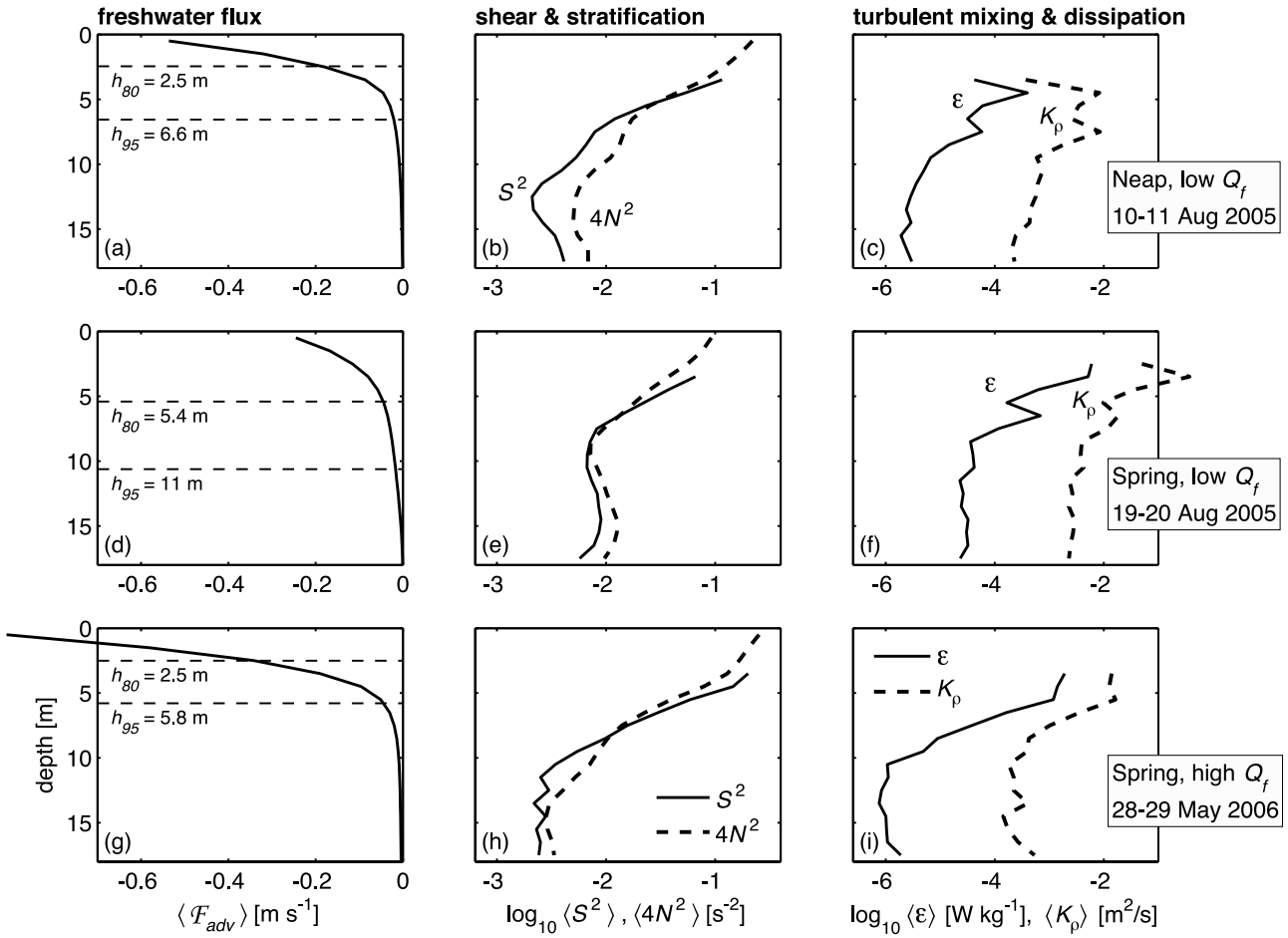

Figure 10. Time-averaged vertical structure in the near-field plume (station P) for the three periods shown in Figure 7. (a, d, g) Freshwater flux (negative offshore) with the plume thickness indicated (h_{80} and h_{95} represent the depths above which 80 or 95% of the freshwater flux is carried, in a time mean sense.) (b, e, h) S^2 and $4N^2$ and (c, f, i) ϵ and K_ρ, averaged over the periods of offshore freshwater flow (i.e., blue in Figure 8b).

5.4. Spatial Structure of the Near-Field Plume

[50] To provide greater context for the present analysis, we combine all transect data to assess whether station P is representative of the larger near-field plume. Here we explore the spatial structure (both along and across the plume axis) of tidally averaged freshwater transport, its median freshness, and the associated turbulence (Figure 11). To help simplify the presentation, we have averaged together tidal cycles that produce a similar magnitude response and spatial distribution. In the following, we summarize salient features of the tidal plume, with a specific goal of putting the results obtained at station P into perspective.

5.4.1. Freshwater Transport

[51] From the spatial distribution of the freshwater advection, we find that station P was located within the core of the tidal plume in 2005. During the downwelling favorable winds in May 2006, the core of the plume was slightly to the north of line 4. Its along-axis decay indicates radial spreading. Freshwater transport depends primarily on the river flow Q_f and to second order on the strength of each ebb pulse (i.e., $\Delta\eta_o$), which alters the amount of fluid expelled from the estuary.

5.4.2. Median Freshness

[52] The median freshness of the freshwater transport has weak spatial variability, and is not particularly sensitive to alignment along the central axis of the plume. We find it is relatively insensitive to the strength of the current ebb, (i.e., the median freshness is similar for consecutive ebbs, even ones with strong diurnal inequality), instead varying seasonally and with the spring/neap cycle. Along-axis decay of freshness is associated with mixing, so cycles with high dissipation (i.e., strong ebbs) generally exhibit a more rapid decay of freshness.

5.4.3. Energy Dissipation

[53] To quantify the bulk energy dissipation of the tidal plume, we compute the mean ϵ between 5 m $< z <$ 15 m at station P during the ~6-h period of each ebb pulse ($\langle \epsilon \rangle_{5-15\mathrm{m}}$), aware of the likelihood that the highest dissipation rates may be confined to the poorly sampled near-surface region we have omitted.

[54] We find that $\langle \epsilon \rangle_{5-15\mathrm{m}}$ has weak or no dependence on Q_f, but instead scales with the strength of the ebb pulse (Figure 12). Ebb strength is characterized in two ways: (1) from the square of the maximum barotropic velocity for

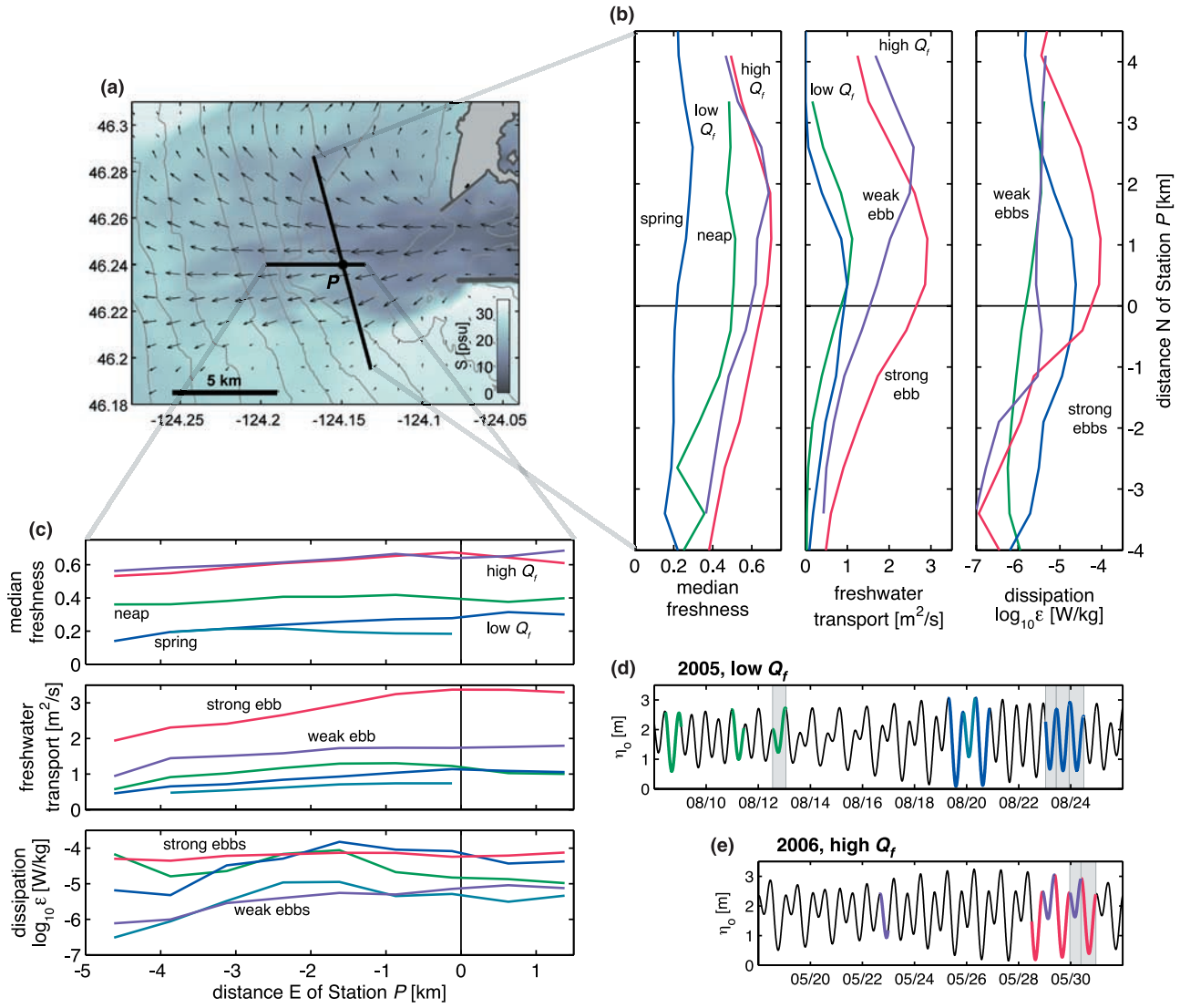

Figure 11. Spatial structure of the near-field tidal plume during different tidal forcings and river flows. (b, c) Median freshness, the depth-integrated freshwater transport (per m in the N–S direction), and the mean turbulent dissipation (averaged between 5 m < z < 15 m over the ebb duration). (d, e) Time series of tidal elevation η_o. To isolate trends, data from similar types of tidal drops and river flows have been averaged together as indicated. Shaded periods in the η_o time series correspond to cross-plume transects (line 1, Figure 11b), and the others correspond to along-axis transects (line 4, Figure 11c). Groupings were chosen that yield similar freshness, transport, and dissipation. For example, green lines in Figure 11c represent means from the two 12.4-h occupations on 8 August 2005 and 11 August 2005, whereas the green lines in Figure 11b represent a single 12.4-h occupation on 12 August 2005. These represent small tidal drops during neap tides and low Q_f; note that the lesser ebb on 20 August 2005 was not averaged with these as it represents a small drop during spring tides, leading to a different median freshness. (a) The plan view shows our transects in relation to surface salinity s and velocity **u** during the greater ebb at 1508 on 20 August 2005 as simulated with Regional Ocean Modeling System [*MacCready et al.*, 2008].

the current ebb at station E, $\max\{u^2_{\mathrm{ebb}}\}$, as predicted using the CORIE simulation databases [*Baptista*, 2006], and (2) from the surface tide as $\Delta\eta_o^2$, the elevation of the previous high tide minus that of the current low, squared. The strong relation using either metric suggests that near-field dissipation depends primarily on the strength of tidal forcing (driving S^2), with stratification effects being secondary. However, because our averaging omits the upper 5 m, a significant fraction of dissipation may be neglected in Figure 12, especially in thin plumes associated with high stratification (neap tides or high Q_f).

[55] We conclude that station P is located within the central flow of the Columbia River plume. Station P appears to be representative of the broader tidal plume for metrics such as the freshness of the median freshwater transport, energy dissipation, etc., so is therefore useful for assessing

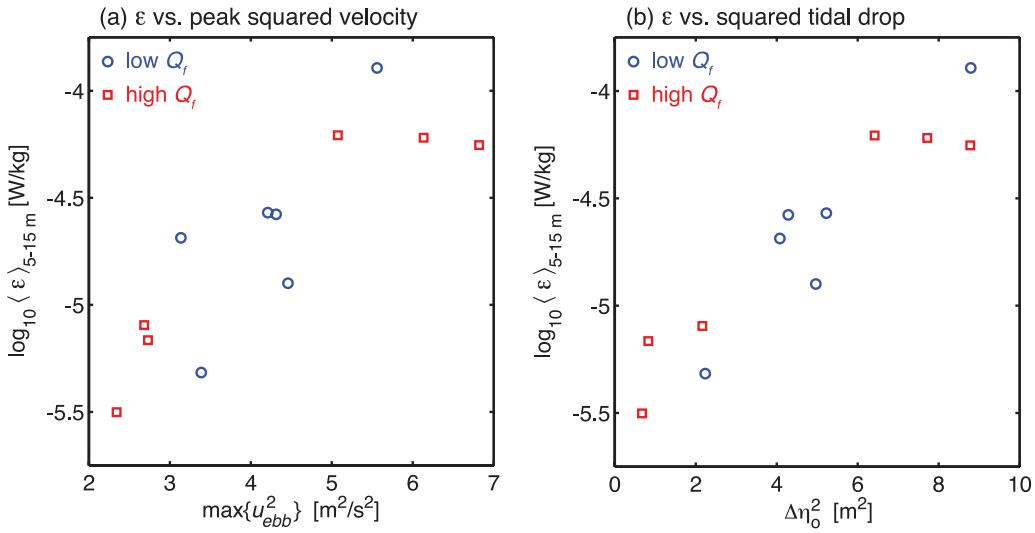

Figure 12. Mean dissipation rate beneath the tidal plume as a function of (a) the square of maximum ebb barotropic velocity ($\max\{u^2_{\text{ebb}}\}$) and (b) the square of surface tidal drop $\Delta\eta_o^2$ for 2005 (circles) and 2006 (squares). $\langle\epsilon\rangle_{5-15\text{m}}$ represents an average of ϵ between 5 m < z < 15 m at station P during the ~6-h period of each ebb pulse.

how plume properties change in response to changes in tidal and river forcing.

6. Linkages to the Large-Scale Forcing

[56] In section 5 we found that seasonal and cycle-to-cycle differences in near-field plume properties appear to vary systematically with tidal forcing and freshwater flow. Here we postulate that the plume structure is controlled by dynamics within the estuary, and suggest that the ratio of horizontal advection to vertical mixing acts as a primary control on the cumulative dilution of river water. For example, if one were to triple the horizontal freshwater transport while maintaining the same vertical turbulent fluxes, the resultant fluid exiting the estuary would be 3 times fresher, assuming the length of mixing wedge remained the same, etc. If we assume that $\mathcal{F}_{\text{adv}}$ scales with Q_f and $\mathcal{F}_{\text{turb}}$ with u^3_{tidal}, then the estuary Richardson number Ri_E, as defined by *Fischer* [1972] represents a nondimensional ratio of turbulent to advective fluxes:

$$Ri_E = g\frac{\Delta\rho}{\rho}\left(\frac{Q_f}{Wu^3_{\text{tidal}}}\right) \tag{4}$$

where g is the gravitational acceleration, $\Delta\rho/\rho = 0.025$ is the fractional density difference between river (fresh) and ocean (salt) water, and $W = 2000$ m is the effective channel width.

6.1. Plume Freshness

[57] To assess whether the near-field composition can be predicted through Ri_E, we compute $\mathcal{F}^{(s)}_{\text{adv}}$ for each of the 17 tidal cycles and use $\overline{\overline{s}}$ to represent the median near-field salinity at station P. Ri_E is computed from Q_f and the tidal velocity u_{tidal} as estimated at station E using the CORIE simulation database [*Baptista*, 2006]. We compute Ri_E on the basis of tidal velocities smoothed over both 12.4- and 24.8-h time scales, the latter which is intended to average over the diurnal inequality and capture the longer–time scale tidal variability (i.e., the spring/neap cycle).

[58] The time evolution of $\overline{\overline{s}}$ and Ri_E^{-1} (Figure 13) exhibits strong covariability between these on both spring/neap and seasonal/yearly time scales. The former results from the u^3_{tidal} dependence, the latter from differences due to Q_f. However, the diurnal inequality strongly affects Ri_E^{-1} on short time scales, producing factor of 2 variability between lesser and greater ebbs. In contrast, $\overline{\overline{s}}$ exhibits very weak diurnal variability, suggesting that the time scale over which estuarine mixing equilibrates is significantly longer than one tidal cycle. Thus, near-field freshness is set by mixing processes that integrate over several-day time scales. This is consistent with the fact that the estuary residence time is 1 to several days, depending on the river flow and tidal strength [*Jay and Smith*, 1990a].

[59] To quantify this covariability, we consider 24.8-h average $\langle Ri_E^{-1}\rangle_{24\text{h}}$ and compare these directly to $\overline{\overline{s}}$ (Figure 14a). Because of the discrete nature of our sampling, the data fall into three groups associated with the three periods shown in Figures 7 and 9 (neap, low Q_f; spring, low Q_f; and spring, high Q_f). Median salinities during May 2006 are distinct from those during August 2005, regardless of tidal strength, i.e., even the weakest neap tides during August 2005 produce a saltier plume (i.e., better mixed), than spring tides during May 2006. However, the trend with $\langle Ri_E^{-1}\rangle_{24\text{h}}$ is consistent even within each group.

[60] The relationship between $\overline{\overline{s}}$ and $\langle Ri_E^{-1}\rangle_{24\text{h}}$ is clearly not linear. This may be rationalized by considering $\overline{\overline{s}}$ for two limiting cases of Ri_E^{-1}. For $Ri_E^{-1} \to 0$, we would expect no mixing and a purely fresh plume ($\overline{\overline{s}} = 0$). For the case of $Ri_E^{-1} \to \infty$, we have either no river input or infinite tidal mixing so that $\overline{\overline{s}} = s_o$. The data presented in Figure 14a appear consistent with these two extremes.

[61] If $\overline{\overline{s}}$ is indeed an appropriate metric to describe plume composition, then the agreement in Figure 14a confirms that the dominant control on the freshness of the near-field plume is a balance between freshwater input and cumulative

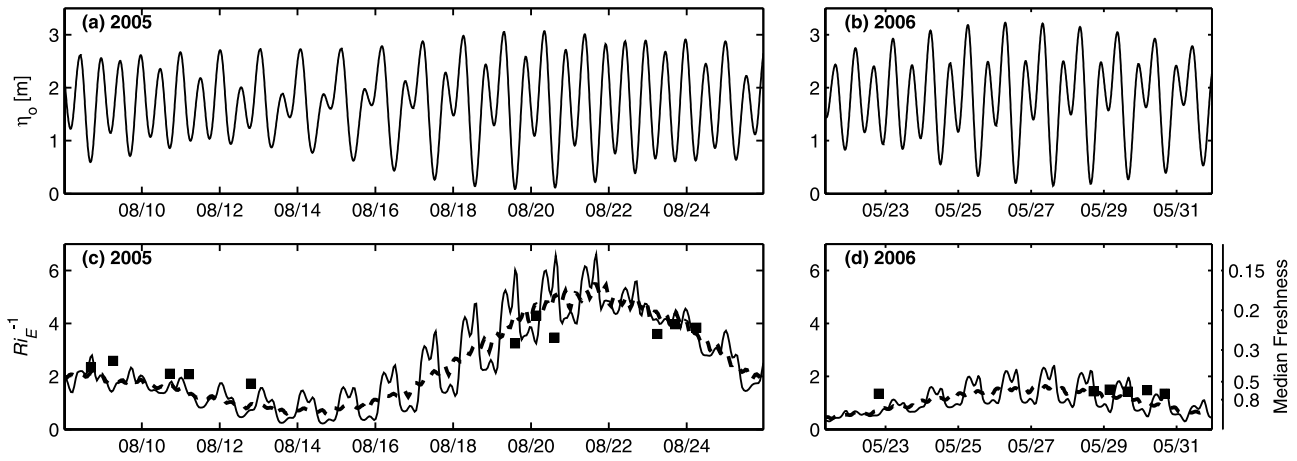

Figure 13. Time series of (a, b) tidal elevation η_o at the North Jetty (from XTide) and (c, d) inverse estuary Richardson number during August 2005 and May 2006. In Figures 13c and 13d, solid and dashed lines represent Ri_E^{-1} filtered at 12.4 and 24.8 h, respectively; also shown is the median freshness (squares; plotted inversely with scale to the right). Ri_E^{-1} was computed at 46°15.2′N, 124°1.4′W using barotropic velocities from the CORIE simulation databases [*Baptista*, 2006] courtesy of Charles Seaton, Yinglong Zhang, and Antonio Baptista.

tidal mixing in the estuary, as represented by an average over several tidal cycles.

6.2. Plume Thickness

[62] As indicated by Figures 7 and 10, the thickness of the near-field plume h_{95} (defined as the depth above which 95% of the time-averaged freshwater flux is transported) is largest during periods of strong mixing and weak river flow. We thus expect plume thickness to increase with increased estuary dilution, and anticipate h_{95} to scale with $\langle Ri_E^{-1}\rangle_{24h}$. We find strong covariance between these (Figure 14b), confirming this assertion. As with $\bar{\bar{s}}$, 24.8-h averaging is required to achieve this agreement because h_{95} exhibits weak diurnal inequality even during periods of strongly unbalanced diurnal tides. This further confirms that mixing processes acting over time scales of several days are important for setting both the plume structure and freshness.

6.3. Turbulent Mixing

[63] Unlike $\bar{\bar{s}}$ and h_{95}, which are set by the cumulative estuarine mixing that occurs over a time scale of several days, turbulence in the near-field plume scales with the strength of the current ebb pulse (Figure 12). On the basis of the scaling in Figure 12, $\langle\epsilon\rangle_{5-15m}$ was found to have no dependence on Q_f, suggesting that ϵ cannot be characterized using Ri_E, which scales with Q_f. In contrast, the eddy diffusivity K_ρ depends on both ϵ and N^2, so has some Ri_E dependence because stratification scales with Ri_E^{-1}. Since

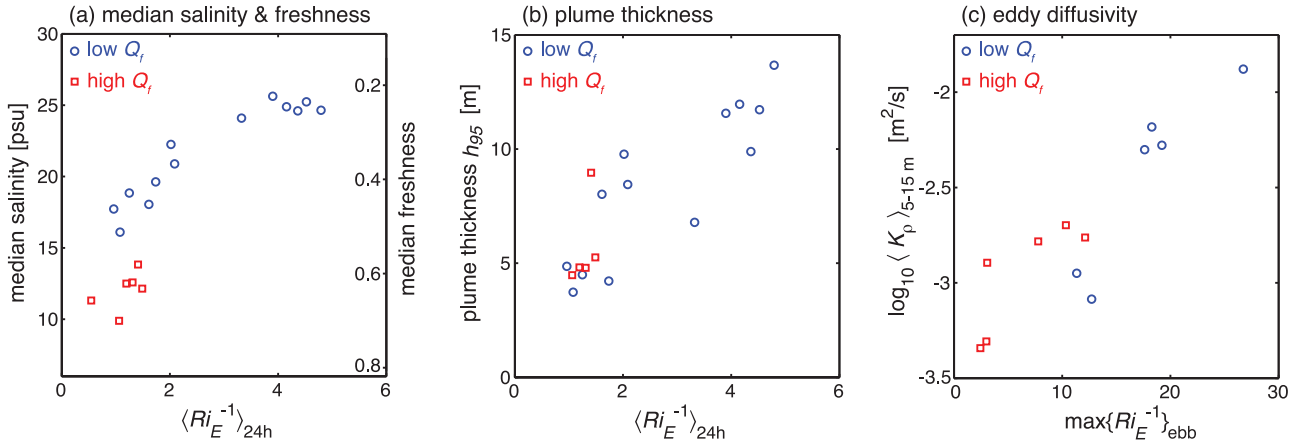

Figure 14. Attributes of the near-field plume as a function of a suitably averaged estuary Richardson number Ri_E for periods of low Q_f (2005, circles) and for high Q_f (2006, squares). (a) Median salinity $\bar{\bar{s}}$ of the near-field freshwater flux, corresponding to the squares in Figure 13, as a function of $\langle Ri_E^{-1}\rangle_{24h}$, with Ri_E^{-1} based on 24.8-h averages of $|u^3_{tidal}|$ (dotted lines in Figure 13), which varies slowly over a time scale of several days. (b) Plume thickness h_{95} as a function of the 24.8-h average $\langle Ri_E^{-1}\rangle_{24h}$; h_{95} represents the depth above which 95% of the time-averaged freshwater flux occurs (Figure 10). (c) Turbulent mixing $\langle K_\rho\rangle_{5-15m}$ as a function of the maximum instantaneous Ri_E^{-1} associated with the current ebb (max$\{Ri_E^{-1}\}_{ebb}$), which characterizes the strength of the outgoing tidal pulse.

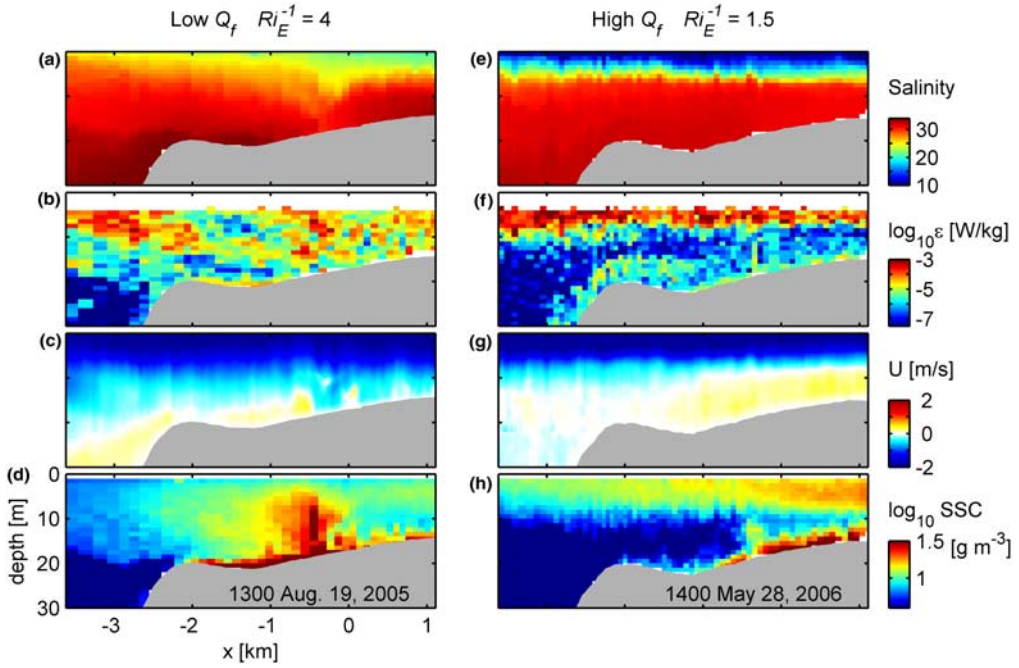

Figure 15. A comparison of the along-axis structure of the offshore plume during (a–d) low Q_f (1400, 19 August 2005) and (e–h) high Q_f (1400, 28 May 2006). Each transect was acquired along line 4 (see Figure 1) during the maximum flow of a greater ebb. Distances are relative to station P.

mixing at the plume base depends on the strength of the ebb, not its longtime average, we seek a dependence of $\langle K_\rho \rangle_{5-15\mathrm{m}}$ on $\max\{Ri_E^{-1}\}_{\mathrm{ebb}}$, the peak Ri_E^{-1} during that ebb pulse. Here we define the diffusivity at the plume base $\langle K_\rho \rangle_{5-15\mathrm{m}}$ as the average between 5- and 15-m water depths during ebb flow. As shown in Figure 14c, data from both field seasons collapse using the above scaling.

7. Conclusions

[64] Because vertically integrated dissipation rates (and hence buoyancy flux) in the Columbia River estuary are primarily driven by tidal stresses, vertical buoyancy fluxes are similar during periods of low and high river discharge. For example, turbulent freshwater fluxes were only 35% higher during our May 2006 sampling, when horizontal freshwater transports were more than a factor of 3 larger than in August 2005. As a result, river dilution (the ratio of turbulent fluxes to advective transports) is dramatically reduced during periods of high river outflow.

[65] The estuary Richardson number (Ri_E) [*Fischer*, 1972] is a useful parameter in quantifying properties of the resultant offshore plume. For this purpose, Ri_E represents a ratio between freshwater advection ($\mathcal{F}_{\mathrm{adv}}$) and mixing ($\mathcal{F}_{\mathrm{turb}}$), with the assumption that advection scales with Q_f and the turbulence scales with u_{tidal}^3. Here we use 17 tidal cycle averages to compute the median salinity $\bar{\bar{s}}$ and thickness h_{95} of freshwater transport offshore in the near-field plume, as well as the mixing at the plume base. On the basis of data from two field seasons with substantially different river flows and a variety of tidal forcings, we find that three critical properties of the near-field river plume are predicted by a suitably averaged Ri_E, as summarized in Figure 14:

[66] 1. The plume's median salinity $\bar{\bar{s}}$ scales with $\langle Ri_E^{-1} \rangle_{24\mathrm{h}}$ (Figures 13 and 14a), the 24.8-h average Ri_E^{-1}. In other words, freshwater dilution depends on a balance between the cumulative estuary mixing (tidally dominated, yet which integrates over several days) and river-supplied freshwater flow.

[67] 2. The plume's thickness h_{95} also scales with the slowly varying $\langle Ri_E^{-1} \rangle_{24\mathrm{h}}$ (Figure 14b), so that highly diluted plumes tend to be thicker, since they have entrained more oceanic fluid and occupy a larger volume.

[68] 3. Turbulent mixing at the plume base, $\langle K_\rho \rangle_{5-15\mathrm{m}}$ scales with $\max\{Ri_E^{-1}\}_{\mathrm{ebb}}$, the peak Ri_E^{-1} during that ebb pulse (Figure 14c). The ebb-averaged TKE dissipation rate $\langle \epsilon \rangle_{5-15\mathrm{m}}$ scales not with Ri_E^{-1}, but instead with the strength of the tidal cycle, as quantified by either $\max\{u_{\mathrm{ebb}}^2\}$ or $\Delta\eta_o^2$ (Figure 12).

[69] We further speculate that the composition, structure and turbulence of other river-plume systems should also be characterized by Ri_E^{-1}, although each river would have its own unique dependencies.

[70] The above processes have dramatic implications to the dynamics and transports within the offshore plume. These are illustrated in Figure 15, which contrasts the salinity, turbulence, velocity and suspended sediment concentration along an E-W line in the plume near field (see Figure 1 for location). Each roughly corresponds to the maximum flow of a greater ebb of similar strength (see Figure 13 for temporal context). For low freshwater input (Figures 15a–15d), the resultant plume is weakly stratified and interacts with the bottom to at least the 20-m isobath. Plume-generated turbulence spans the water column, permitting strong sediment resuspension events (Figure 15d) with associated geochemical impacts; these are documented by Spahn et al. (submitted manuscript, 2008). In contrast,

high river flows produce a strongly stratified plume that detaches from the bottom farther upstream. During these periods, turbulence is more intense but confined to the upper 10 m. These differences may have significant dynamical implications, as high, near-surface stratification traps Ekman transports, and may cap or retain biologically active regions.

[71] **Acknowledgments.** We thank Mike Neeley-Brown, Ray Kreth, and Sasha Perlin for their technical expertise and Sam Kelly, Greg Avicola, Robin Bjorkquist, Denis Franklin, Alex Horner-Devine, Emily Spahn, and the captain and crew of the R/V *Pt. Sur* for making the data collection possible. Helpful comments were provided by David Jay and Jim Lerczak. We thank Parker MacCready and Charles Seaton for kindly providing numerical model output. The suggestions of two anonymous reviewers greatly improved this paper. This research was funded by NSF OCE-0238727.

References

Baptista, A. (2006), CORIE: The first decade of a coastal-margin collaborative observatory, in *Oceans 2006*, pp. 1–6, Inst. of Electr. and Electr. Eng., Piscataway, N. J.

Chant, R., W. Geyer, R. Houghton, E. Hunter, and J. Lerczak (2007), Estuarine boundary layer mixing processes: Insights from dye experiments, *J. Phys. Oceanogr.*, *37*, 1859–1877.

Dillon, T. M. (1982), Vertical overturns: A comparison of Thorpe and Ozmidov length scales, *J. Geophys. Res.*, *87*, 9601–9613.

Fischer, H. B. (1972), Mass transport mechanisms in partially stratified estuaries, *J. Fluid Mech.*, *53*, 671–687.

Fong, D. A., and W. R. Geyer (2001), Response of a river plume during and unpwelling favorable wind event, *J. Geophys. Res.*, *106*, 1067–1084.

Geyer, W. R., and J. D. Smith (1987), Shear instability in a highly stratified estuary, *J. Phys. Oceanogr.*, *17*, 1668–1679.

Geyer, W. R., J. H. Trowbridge, and M. M. Bowen (2000), The dynamics of a partially mixed estuary, *J. Phys. Oceanogr.*, *30*, 2035–2048.

Horner-Devine, A. R. (2009), The bulge circulation in the Columbia River plume, *Cont. Shelf Res.*, *29*, 234–251, doi:10.1016/j.csr.2007.12.012.

Horner-Devine, A., D. Jay, P. Orton, and E. Spahn (2008), A conceptual model of the strongly tidal Columbia River plume, *J. Mar. Syst.*, doi:10.1016/j.jmarsys.2008.11.025, in press.

Jay, D. A. (1991), Internal asymmetry and anharmonicity in estuarine flows, in *Progress in Tidal Hydrodynamics*, edited by B. B. Parker, pp. 521–543, John Wiley, New York.

Jay, D. A., and J. D. Musiak (1996), Internal tidal asymmetry in channel flows: Origins and consequences, in *Mixing Processes in Estuaries and Coastal Seas*, *Coastal Estuarine Sci.*, vol. 50, edited by C. Pattiaratchi, pp. 219–258, AGU, Washington, D. C.

Jay, D. A., and J. D. Smith (1990a), Circulation, density distribution and neap-spring transitions in the Columbia River estuary, *Prog. Oceanogr.*, *25*, 81–112.

Jay, D. A., and J. D. Smith (1990b), Residual circulation in shallow, stratified estuaries. II. Weakly-stratified and partially-mixed systems, *J. Geophys. Res.*, *95*, 733–748.

Kay, D. J., and D. A. Jay (2003), Interfacial mixing in a highly stratified estuary 1. Characteristics of mixing, *J. Geophys. Res.*, *108*(C3), 3072, doi:10.1029/2000JC000252.

Kudela, R. M., and T. D. Peterson (2009), Influence of a buoyant river plume on phytoplankton nutrient dynamics: What controls standing stocks and productivity?, *J. Geophys. Res.*, *114*, C00B11, doi:10.1029/2008JC004913.

Lentz, S. J. (2004), The response of buoyant coastal plumes to upwelling-favorable wind, *J. Phys. Oceanogr.*, *34*, 2458–2469.

Lerczak, J. A., W. R. Geyer, and D. K. Ralston (2008), The temporal response of the length of a partially-stratified estuary to changes in river flow and tidal amplitude, *J. Phys. Oceanogr.*, *39*, 915–933.

Li, M., J. Trowbridge, and R. Geyer (2008), Asymmetric tidal mixing due to the horizontal density gradient, *J. Phys. Oceanogr.*, *38*, 418–434.

Lohan, M. C., and K. W. Bruland (2006), Importance of vertical mixing for additional sources of nitrate and iron to surface waters of the Columbia River plume: Implications for biology, *Mar. Chem.*, *98*, 260–273.

MacCready, P., N. Banas, B. Hickey, E. Dever, and Y. Liu (2008), A model study of tide-and wind-induced mixing in the Columbia River Estuary and plume, *Cont. Shelf Res.*, *29*, 278–291, doi:10.1016/j.csr.2008.03.015.

MacDonald, D. G., and W. R. Geyer (2004), Turbulent energy production and entrainment at a highly stratified estuarine front, *J. Geophys. Res.*, *109*, C05004, doi:10.1029/2003JC002094.

MacDonald, D. G., and A. R. Horner-Devine (2008), Temporal and spatial variability of vertical salt flux in a highly stratified estuary, *J. Geophys. Res.*, *113*, C09022, doi:10.1029/2007JC004620.

MacKinnon, J. A., and M. C. Gregg (2003), Mixing on the late-summer New England shelf — Solibores, shear, and stratification, *J. Phys. Oceanogr.*, *33*, 1476–1492.

Moum, J. N., M. C. Gregg, R. C. Lien, and M. Carr (1995), Comparison of turbulence kinetic energy dissipation rate estimates from two ocean microstructure profilers, *J. Atmos. Oceanic Technol.*, *12*, 346–366.

Moum, J. N., D. M. Farmer, W. D. Smyth, L. Armi, and S. Vagle (2003), Structure and generation of turbulence at interfaces strained by internal solitary waves propagating shoreward over the continental shelf, *J. Phys. Oceanogr.*, *33*, 2093–2112.

Nash, J. D., and J. N. Moum (2005), River plumes as a source of large amplitude internal waves in the coastal ocean, *Nature*, *437*, 400–403, doi:10.1038/nature03936.

Osborn, T. R. (1980), Estimates of the local rate of vertical diffusion from dissipation measurements, *J. Phys. Oceanogr.*, *10*, 83–89.

Peters, H. (1997), Observations of stratified turbulent mixing in an estuary: Neap-to-spring variations during high river flow, *Estuarine Coastal Shelf Sci.*, *45*, 69–88.

Peters, H., and R. Bokhorst (2000), Microstructure observations of turbulent mixing in a partially mixed estuary. Part I: Dissipation rate, *J. Phys. Oceanogr.*, *30*, 1232–1244.

Peters, H., and R. Bokhorst (2001), Microstructure observations of turbulent mixing in a partially mixed estuary. Part II: Salt flux and stress, *J. Phys. Oceanogr.*, *31*, 1105–1119.

Simpson, J. H., J. Brown, J. Matthews, and G. Allen (1990), Tidal straining, density currents, and stirring in the control of estuarine stratification, *Estuaries*, *13*, 125–132.

Stacey, M., and D. Ralston (2005), The scaling and structure of the estuarine bottom boundary layer, *J. Phys. Oceanogr.*, *35*, 55–71.

Stacey, M. T., S. G. Monismith, and J. R. Burau (1999), Observations of turbulence in a partially stratified estuary, *J. Phys. Oceanogr.*, *29*, 1950–1970.

Trowbridge, J. H. (1992), A simple description of the deepening and structure of a stably stratified flow driven by a surface stress, *J. Geophys. Res.*, *97*, 15,529–15,543.

Trowbridge, J. H., W. R. Geyer, M. M. Bowen, and A. J. Williams (1999), Near-bottom turbulence measurements in a partially mixed estuary: Turbulent energy balance, velocity structure, and along-channel momentum balance, *J. Phys.*, 3056–3072.

L. F. Kilcher, J. N. Moum, and J. D. Nash, College of Oceanic and Atmospheric Sciences, Oregon State University, 104 COAS Administration Building, Corvallis, OR 97331, USA. (nash@coas.oregonstate.edu)